Turbulence Embedded Into the Ionosphere by Electromagnetic Waves

Magnus F. Ivarsen[1,2] [ID], **Megan D. Gillies[3]** [ID], **Devin R. Huyghebaert[2,4]** [ID], **Jean-Pierre St-Maurice[2,5]** [ID], **Adam Lozinsky[2]** [ID], **Draven Galeschuk[2]**, **Eric Donovan[3]**, and **Glenn C. Hussey[2]** [ID]

[1]Department of Physics, University of Oslo, Oslo, Norway, [2]Department of Physics and Engineering Physics, University of Saskatchewan, Saskatoon, SK, Canada, [3]Department of Physics, University of Calgary, Calgary, AB, Canada, [4]Department of Physics and Technology, UiT The Arctic University of Norway, Tromsø, Norway, [5]Department of Physics and Astronomy, University of Western Ontario, London, ON, Canada

Abstract When charged particles are accelerated from Earth's magnetosphere and precipitate into the atmosphere, their impact with neutral gas creates the aurora. Structured electric fields drive the acceleration processes but they are also passed down to the ionosphere, meaning that turbulence can in part be *embedded* into the ionosphere rather than emerge through instability processes locally. Applying a point-cloud analysis technique adapted from observational cosmology, we show how observed turbulence in the ionosphere matches electrical current signatures in the pulsating aurora in a series of conjunctions between space- and ground-based instruments. We propose that the temporal spectrum of pulsations in the pulsating aurora is the driver of a clearly observed energy injection into the ionosphere's unstable bottomside. Precipitating electrons produce electric fields through charge deposition, and we observe wave characteristics that are present in this pattern. Next, the relative electron-ion drifts excite the Farley-Buneman instability, the distribution of whose waves are organized according to the local electric field. It is the temporal characteristics of chorus wave interactions in the magnetosphere that is imparted, via precipitating electrons, to the pulsating aurora, and so we propose that chorus wave interactions are capable of embedding turbulent structure into the ionosphere. This structure (now pressure gradients) dissipate energy in the E-region through turbulent processes, observed by the ICEBEAR coherent scatter radar.

1. Introduction

Pulsating Aurora (PA) is a type of auroral phenomenon characterized by quasi periodic modulations or auroral patches with a periodicity of 2–20 s (see, e.g., Lessard, 2012, for a review]. It is a long-lived (several hours) and frequent type of aurora, occurring almost every night (Grono & Donovan, 2020). The PA is mainly observed within regions of diffuse aurora. The pulsating patches are relatively large, some times covering hundreds of kilometres, and their shape can vary over the course of minutes (Grono & Donovan, 2018). Displays of aurora are always caused by accelerated particles that precipitate into Earth's atmosphere, and the PA is in this regard associated with particularly high-energy electron precipitation (10–100 keV of particle kinetic energy), usually on the equatorward edge of the auroral oval (Bland et al., 2021; Nishimura et al., 2020). The precipitation that drives the pulsating aurora tends to be harder (higher particle kinetic energies) and more intense during times of elevated auroral electrojet amplitude (Hosokawa & Ogawa, 2015). Since enhancements in the auroral electrojet are typically driven by the substorm cycle, the PA is often found to occur during the magnetospheric substorm recovery phase. However, the association may not be indicative of a causal relationship (Jones et al., 2011).

The source of the PA's energetic electrons has been traced to chorus wave activity in the magnetosphere which allows for these energetic electrons originating in the radiation belts to be scattered into the ionosphere via the loss cone (Kasahara et al., 2018). The pulsations, and their corresponding fast sub-pulsations, are themselves closely linked to the dynamic behavior of magnetospheric chorus waves, with a matching temporal signature observed down to sub-second fluctuations (Hosokawa et al., 2020a). The internal and external structure of the pulsating patches are closely linked to field-aligned current (FAC) amplitude (Gillies et al., 2015; Hosokawa & Ogawa, 2010). A general overview of these processes are shown in Figure 1a.

The abundant sub-pulsations of the pulsating aurora will thus lead to structuring, or filamentation, in the FACs. Such structured FACs are in turn associated with highly structured electric fields, representing a strong energy
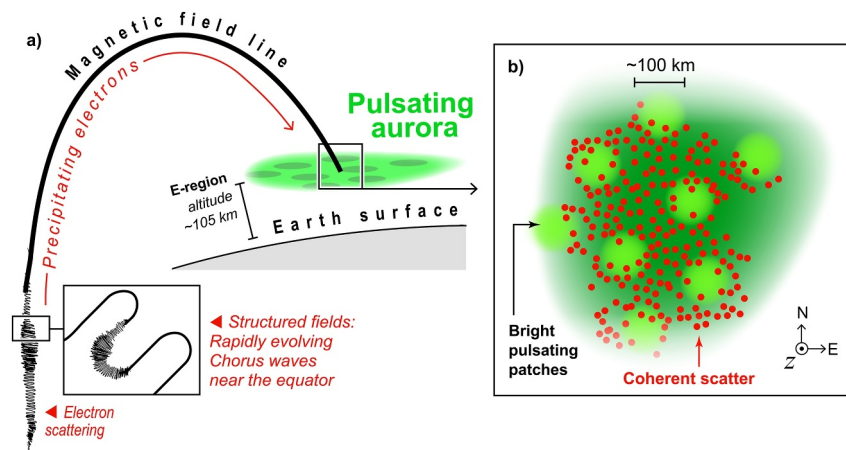
Figure 1. Panel (a): A schematic representation of a closed magnetic field line connecting the auroral E-region to the magnetosphere, where chorus wave-particle interactions are causing electrons to precipitate, creating the pulsating aurora. This region is located near magnetic equator. Panel (b): a close-up schematic view of the E-region during pulsating auroral emissions (green patches), with coherent backscatter echoes (small-scale irregularities) in red circle points, where the regions surrounding the pulsating patches.

transfer from the magnetosphere to the ionosphere, quantified by the downard Poynting flux (Billett et al., 2021; Taguchi et al., 1995).

The subsequent modulations in plasma density, field strength, and conductivity are known to produce small-scale turbulence in the E-region, observable with SuperDARN radars (Hosokawa, Motoba, et al., 2010; Milan et al., 2008). In Figure 1b, which expands upon a portion of panel a), these turbulence echoes are denoted by red circle points, and we expect them to cluster *between* auroral patches, since that is where backscatter power maximizes (Hosokawa, Motoba, et al., 2010). Outside of the pulsating patches are also the regions where FACs typically maximize (Gillies et al., 2015). In the present report, using 3D coherent scatter radar data with an unprecedented spatial resolution, we demonstrate during a strong PA event that there is a clear turbulent signal observable in the ionospheric plasma that matches the structured FACs from above in detail. A turbulent ionospheric "surface" consequently oscillates in tandem with the pulsating aurora, much like an electrical drum-skin.

PA-associated plasma turbulence is most evident during extreme storm-time disturbances in Earth's geospace (Milan et al., 2008), when the entire ionosphere can be highly structured, with widespread plasma turbulence at high latitudes (Huba et al., 1985). During such periods, the solar wind is pushing against Earth's magnetosphere, and irregularities grow *locally* through instability processes caused by electric fields, plasma convection, and sharp gradients in plasma density (Tsunoda, 1988). On the other hand, processes in the magnetosphere can impart structure on the ionosphere that is not driven locally, through highly structured electric and magnetic fields that get passed down along Earth's field lines (Keiling et al., 2019), by causing filamentary structuring of the plasma through magnetic pressure gradients (Laundal et al., 2019), by the production of plasma waveforms (Rinnert, 1992), or by general periodic modulations of the ionospheric electric field (Foster & Tetenbaum, 1992). Although a variety of high-latitude turbulence-generating mechanisms are known, little is known specifically about when and how any one process is dominant (Ivarsen, Jin, et al., 2023).

Indeed, the study of turbulence is notoriously *difficult* (Feynman & Sands, 1963). *In-situ* measurements by spacecraft have proven an essential way to understand ionospheric plasma turbulence on scales ranging from ~1 cm up to 100 km (Basu et al., 1984; Jin et al., 2021; Kintner & Seyler, 1985; Lorentzen et al., 2010; Mounir et al., 1991; Spicher et al., 2022). However, spacecraft move fast with respect to the plasma and can only provide a transient picture of the evolving turbulence. In this regard, recent advances in coherent scatter radar technology allows for an efficient, continuous monitoring of km-scale plasma density irregularities. The Canadian ICEBEAR 3D radar is capable of imaging the E-region irregularity field, providing a *spectrum* of turbulence-echo clustering for field-perpendicular scale sizes between 1 and 25 km (Ivarsen, Lozinsky, et al., 2023; Ivarsen, St-Maurice, Hussey, Spicher, et al., 2023). Being ground-based, ICEBEAR 3D can characterize turbulent shapes in the ionosphere over arbitrarily long timescales within the field-of-view of the radar.

Leveraging *in-situ* (Swarm), ground-based observations of turbulent structuring in the auroral ionosphere (ICEBEAR 3D), and optical measurements of the pulsating aurora (TREX RGB), we present a ~25 min event where intense PA coincides with a clear injection of energy into the ionospheric irregularity field. We analyze radar observations of E-region Farley-Buneman (Buneman, 1963; FB, Farley, 1969) waves statistically, and together with observations of field-aligned current structuring, we independently confirm that this injection takes place on spatial scales between 2 and 5 km. The pulsations in the PA are produced locally through impacting electrons, and these impacts serve also to deposit charge, modulating the ionospheric electric field. The modulations cause a periodic and characteristic pattern in the perpendicular electric field in the E-region. Given that the PA's pulsations originate in the wave characteristics of *chorus waves*, we are able to trace the stochastic properties of E-region turbulence back to the magnetosphere. This allows for the process in which electromagnetic waves excite perpendicular propagating waves in the E-region (Foster & Tetenbaum, 1992; Rinnert, 1992) to function at a distance, with the electron precipitation in the pulsating aurora as a mediator.

2. Methods

The pulsating aurora event presented in this report was fortuitously observed simultaneously by a range of instruments, allowing for a comprehensive analysis of the event. The main instruments used in this study are ICEBEAR, TREX RGB and Swarm.

2.1. Coherent Scatter Radar Data

ICEBEAR is a coherent scatter radar operating with a center frequency of 49.5 MHz located in Saskatchewan, Canada (Huyghebaert et al., 2019, 2021). The radar makes measurements of ~3 m plasma density irregularities over an approximately 600 km × 600 km field-of-view in the auroral region with a temporal resolution of 1 s and a spatial resolution of 1.5 km. The measurements are mapped to the field-of-view using interferometry at the receiver site, providing the scattering locations in 3D (Lozinsky et al., 2022). Whereas the 3 m Farley-Buneman waves observed by the radar nominally yield information (backscatter power, Doppler shift, Doppler spectra) about *small-scale* turbulence in the E-region, we are here using the radar echoes as tracers of larger scale (1–25 km) structures. The method by which this is achieved involves correlating the positions of individual turbulence echoes, using statistical methods adapted from observational cosmology (Ivarsen et al., 2016). What follows is a summary of the method that is described in detail in Ivarsen, Lozinsky, et al. (2023). The method's central observable quantity is $\xi(r)$, the two-point correlation function. It is an auto-correlation function, and it is defined as,

$$n^2[1 + \xi(r)] = \langle \rho(x)\rho(x + r)\rangle, \tag{1}$$

where n is the average number density of echoes in the volume occupied by the echo population under consideration, and $\rho(x)$ is the number density of echoes at location x. r is a distance away from x. We assume statistical homogeneity in the echo population, so that r is a one-dimensional displacement, and the Fourier analysis to be performed obeys rotational symmetry. Inspecting Equation 1 we note that ξ can be interpreted as the fluctuating part of the auto-correlation function, with n^2 as a floor.

The process of calculating ξ and obtaining spectra can be summarized in a few steps. For spatially distinct echo populations.

1. Count echo pairs at spatial separations r, and apply the Monte-Carlo-based Landy-Szalay estimator (Eqs. 8 and 9 in Ivarsen, Lozinsky, et al., 2023) to obtain $\xi(r)$.
2. Apply the inverse Hankel transform to ξ (Eq. 7 in Ivarsen, Lozinsky, et al., 2023). As this transformation involves integration over Bessel functions that oscillate around zero, great care must be taken at this step, using numerical recipes developed for Bessel function integrals (Guizar-Sicairos & Gutiérrez-Vega, 2004).
3. Multiply the spectra by the number of echoes contained in the calculation of that spectrum. This normalization factor does not affect spectral shape or slope, and ensures that integrated spectral power exhibits similar distributions in geomagnetic activity as that of F-region density spectra (Figure 6 in Ivarsen, St-Maurice, Hussey, Spicher, et al., 2023). Power per wavenumber then has the unit of m^{-3}.

The resulting power spectral density curves we dub E-region, or Farley-Buneman, *clustering spectra*. Their spectral shapes and log-log linear slopes have been shown to match the spectrum of field-aligned current structuring, or filamentation, as measured from space (Ivarsen, Lozinsky, et al., 2023), as well F-region density spectra measured *in-situ* (Ivarsen, St-Maurice, Hussey, Spicher, et al., 2023). As the pulsating aurora is typically distributed over a large spatial area, all spectra presented in this study are composite spectra from taking the mean of all distinct echo populations within ICEBEAR's field-of-view.

Regarding altitudes, which are determined through the measured elevation angles of each imaged echo, the ICEBEAR 3D echoes recorded during the event under consideration have a mean altitude of 107 km with a standard deviation of 16 km. As a direct comparison to the average pulsating aurora, Kawamura et al. (2020) finds on average that the PA emissions during magnetic midnight originate from an altitude of 107 km, with standard deviation 12 km. The altitude distribution of the ICEBEAR 3D echoes is in other words strikingly similar to that expected for the PA. Note that we exclude ICEBEAR 3D altitudes from the west-most azimuths, which are anomalous (Ivarsen, St-Maurice, Hussey, Galeschuk, et al., 2023).

2.2. Optical Images of the Aurora

The optical images used in this study are from the TREX (Transition Region Explorer) RGB (red-green-blue) all-sky imager (ASI) located at the Rabbit Lake research station in Northern Saskatchewan, Canada (58.22°N, 103.68°W). The TREX RGB imager is thus located near the middle of ICEBEAR's field-of-view. The TREX RGB ASI is a highly sensitive true-color imager that is designed to capture full-color images of the aurora and airglow (Gillies et al., 2020). Images are produced at 3 s intervals and recorded on a 558×480 pixel resolution CCD. For comparison with ICEBEAR and Swarm data, the CCD pixels are converted to geomagnetic latitude and longitude locations using the Altitude-adjusted Corrected Geomagnetic Coordinate (Baker & Wing, 1989) reference frame for further analysis. We assume an overall emission altitude of 110 km.

2.3. In Situ Satellite Observations

In the present report, we present three conjunctions between satellites from the European Space Agency (ESA) and the Rabbit Lake research station, on 28 August 2021. The satellites in question belong to ESA's Swarm mission (Friis-Christensen et al., 2006). Swarm B orbits Earth at an altitude of around 500 km in the F-region ionosphere, whereas Swarm A and C orbit at around 450 km altitude. All satellites carry a broad range of scientific instruments. We use 50 Hz B-field data from the on-board Vector Field Magnetometer, along with 2 Hz plasma density and temperature measurements from Swarm's Langmuir probe. To show magnetic field data, we use mean-field aligned (MFA) coordinates (Ivarsen et al., 2020; Park et al., 2017). This entails rotating the data from satellite-track coordinates (x along-track, y cross-track, z vertical) into mean-field aligned (MFA) coordinates. The final coordinate system has z in the direction of the mean field (determined by the aforementioned Savitzky-Golay filter), x magnetically north, and y magnetically east. Fluctuations in the east and meridional components correspond directly to structuring in the field-aligned currents present at that location (Ritter et al., 2013).

Figure 2 gives an overview of the instruments used in the present report, as well as showing the local geomagnetic volume above Rabbit Lake in Northern Saskatchewan, Canada. Panel a shows this location in geomagnetic coordinates. Panel b shows an example RGB TREX image, with the visual signatures of the pulsating aurora indicated. Panel c shows how this RGB image appears when wrapped to a shell of altitude 110 km, which is in turn transformed to geomagnetic coordinates, ensuring that the vertical direction in our plots (which involve several altitudes) are field-aligned. As such, geomagnetic west is to the left in Figure 2c. Several detrimental features are indicated, such as trees along the western horizon, clouds to the south-east, and bright moonlight to the east. Nevertheless, the auroral images conclusively show that the PA is active in the southern part of Figure 2c throughout the interval considered (see Supporting Information video). A shaded red area indicate the scan area of a keogram to appear later.

3. Results

Figure 3a shows a synopsis of geospace above Rabbit Lake. Here, the locations of 709,000 individually imaged coherent scatter echoes from ICEBEAR 3D are plotted as green dots. Superposed, the effective pixel size of the remapped RGB TREX image, caused by perspective distortion in the camera lens, is shown by solid red contour lines.
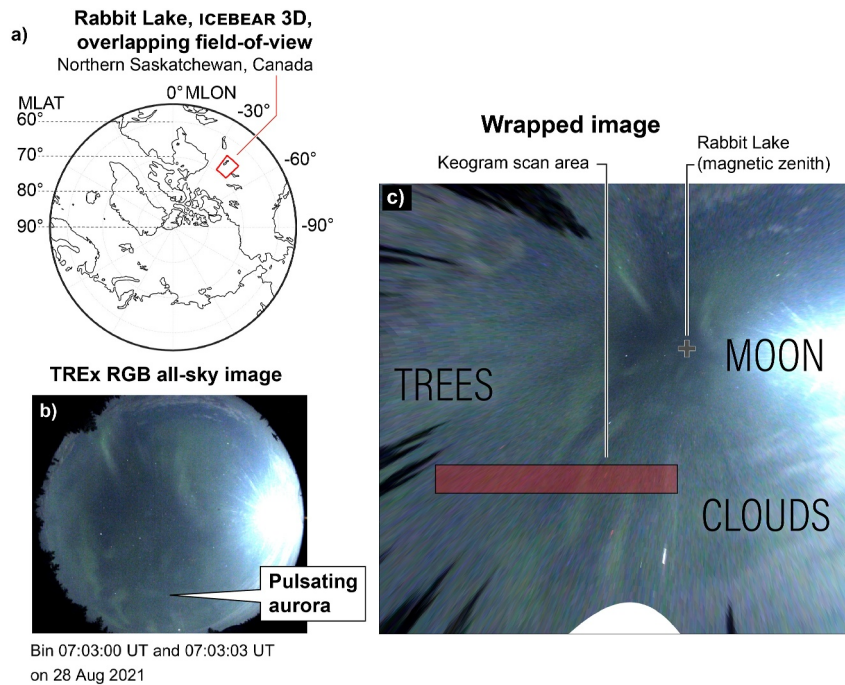
Figure 2. Panel (a): map of the northern high-latitude region under study, with the Rabbit Lake TREX RGB and ICEBEAR 3D overlapping field-of-view indicated. Panel (b): example all-sky-image produced with the TREX RGB imager. Panel (c): the same image, re-mapped to geomagnetic coordinates. Various features are highlighted; a red shaded rectangle indicates the scan area of a keogram that appears in Figure 4.
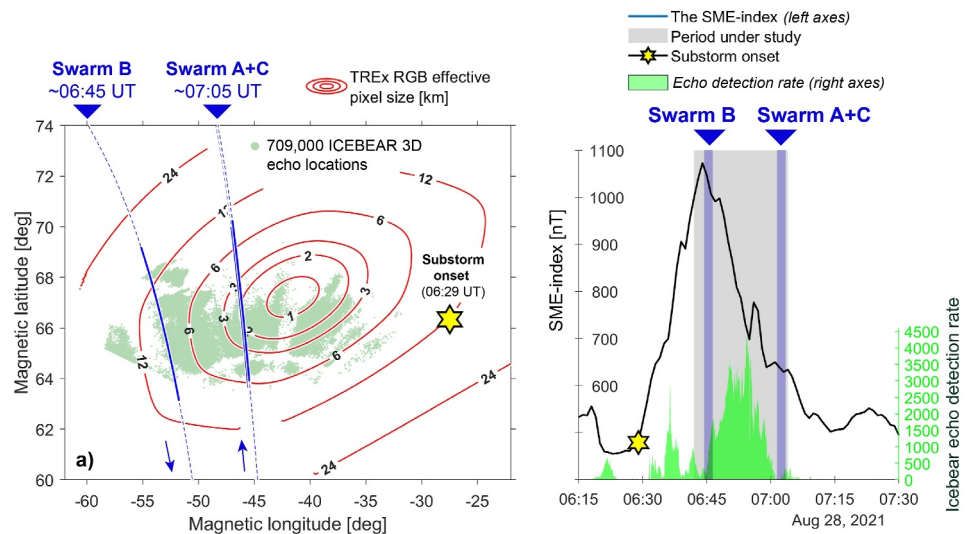
Figure 3. Spatial (panel a) and temporal (panel b) overview of the multiple conjunctions analyzed in the present paper. Panel (a): the blue dashed lines show the Swarm orbits, with the thicker line indicating conjunctions. The red lines show contours of constant RGB TREX effective pixel size (due to perspective distortion in the camera lens), while the light green dots indicate the locations of ICEBEAR 3D echoes. Panel (b): the SME-index for an extended time-interval centered on the conjunctions (gray shaded area). The two blue shaded columns indicate the time of the two conjunctions. The green shaded area (right axis) shows ICEBEAR 3D echo detection rates. In both panels, the footprint onset of a magnetospheric substorm, which is close in time and space to the conjunctions, is indicated by a yellow star.

Dashed blue lines indicate the orbital trajectory of Swarm (at altitudes between 450 and 500 km), again accounting for the field-parallel distance from Swarm altitudes to the E-region and to the ground with geomagnetic coordinates. The thicker, solid blue lines indicate the portions of the Swarm orbits that are considered as conjunctions, each of 105 s duration. Note that the shape of the green echo distribution in Figure 3a is due to the radar gain pattern, in which spurious echoes appear outside of the radar's three main beams (Ivarsen, St-Maurice, Hussey, Galeschuk, et al., 2023). In the two-point correlation analysis of echo locations to be presented, we remove these low-power spurious echoes.

Finally, in Figure 3b the blue line (left y-axis) shows the SME-index between 06:15 UT and 07:30 UT, with the timing of the conjunctions indicated with the blue shaded columns. The SME-index is an auroral electrojet index, and an excellent indicator of geomagnetic activity at high latitudes (Newell & Gjerloev, 2011a). In green shaded area (right y-axis), we show the rate of detected ICEBEAR 3D echoes (per second). In both panels of Figure 3, a yellow star indicates the footprint position (panel a) and onset time (panel b) of a magnetospheric substorm (23.8 hr MLT), found by substorm identification methods (Forsyth et al., 2015; Newell & Gjerloev, 2011b). Around 900 km east of the conjunctions (outside the FOV offered by the auroral imager), we would find the footprint of a substorm that was initiated around 15 min before the first Swarm conjunction. The first conjunction occurred during peak SME expansion, while the second and third conjunctions occur just after the recovery phase of the substorm.

A video is provided in the Supporting Information that shows all three conjunctions, superposed on auroral images and ICEBEAR 3D echo locations. See the Supporting Information for a description of this video.

3.1. Temporal Fluctuations

First, we shall analyze the temporal evolution in the ICEBEAR 3D echo detection rate (cadence 1 s), as well as the RGB TREX auroral images (cadence 3 s). For ICEBEAR, we simply record the number of turbulence echoes detected per second. From the optical images, we will extract a timeseries from the RGB TREX images through the use of a keogram. We subject both timeseries to a temporal power spectral density analysis, which characterizes the intensity of fluctuations present in the timeseries for a range of frequencies (timescales). From Figure 3a we see that the ICEBEAR 3D echoes are aligned longitudinally with the auroral imager field-of-view, and so we opt to calculate a longitudinal keogram (red shaded area in Figure 2c).

Figure 4a shows how the two timeseries evolve, comparing the %-change within a rolling 15-min window, for both timeseries. Panel b) shows a sample cross-correlation of the two quantities, in which one timeseries is correlated against the other with a series of time-shifts (lags) between them. For the case at hand, the panel g) shows that when shifting the emission intensity timeseries 6 min backwards, a positive correlation of around 0.5 is achieved, compared to a *negative* correlation of ∼−0.4 when no timeshift is applied. That is, there is a weak but measurable tendency for the timeseries to anti-correlate, which is likewise clearly discernible in Figure 4a. Moderate correlation is achieved by shifting the RGB data backwards by 6 min. Finally, panel c) shows power spectral density for both timeseries, where we apply both a Lomb-Scargle periodogram (VanderPlas, 2018) and a modified version of Welch's method (Tröbs & Heinzel, 2006). Two broad peaks are identified with a shaded blue area, with their periods (35 and 20 s) indicated in blue. These are likely the primary auroral pulsation periods.

Essentially, Figure 4 details the manner in which two completely different quantities evolve in time. Despite fundamental differences, a cross-correlation analysis confirms that the timeseries are anti-correlated, and power spectral density analysis confirms that they oscillate at similar frequencies. In other words, the emissions intensity fluctuations and the turbulent echo detection rate share key statistical properties. In the language of Hosokawa, Tsugawa, et al. (2020), the field of Farley-Buneman waves in the E-region are reverberating with the "beat" of the pulsating aurora. In a more technical sense, we conclude that both quantities vary, in tandem, in a *stochastic fashion*. Given that the auroral pulsations captured by the keogram ultimately stem from intermittencies in the wave-particle interactions in the magnetosphere (Kasahara et al., 2018), it is tempting to posit that the stochastic variation in both timeseries stem from (possibly non-linear) processes in the magnetosphere. Throughout the remainder of the present paper, we shall substantiate this claim.

Returning to Figure 4b, we recall the tendency for the quantities in panel a to anti-correlate with one another. Again evoking the language of Hosokawa, Tsugawa, et al. (2020), the pulsating aurora and the E-region
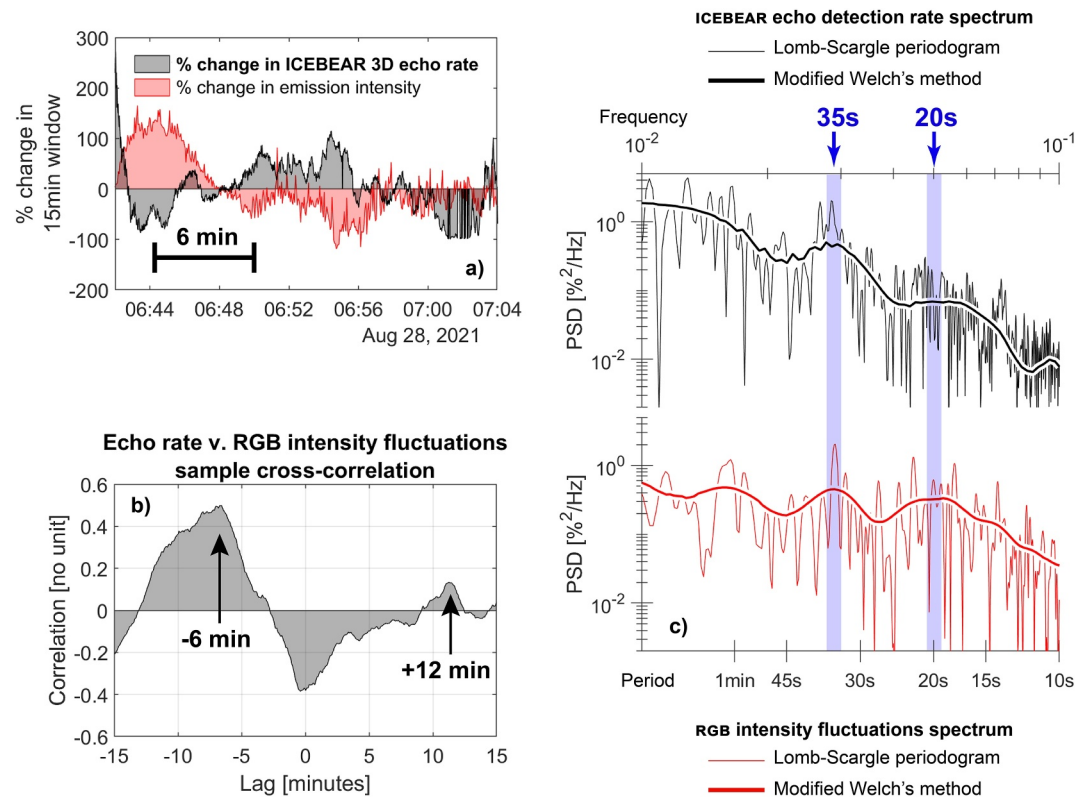
Figure 4. Panel (a) shows the %-change in RGB emission intensity (red) and the %-change in ICEBEAR echo detection rate, both within a 15-min rolling window. The keogram rate of change is amplified by a factor 13 to bring both timeseries at parity. Panel (b) shows the result of a sample cross-correlation of the two timeseries (shifting the keogram by indicated time lags, then correlating the timeseries). Panel (c) shows power spectral density for both timeseries, after applying a 9-s low-pass filter and a 2-min high-pass filter. Thin lines show Lomb-Scargle periodograms while thick lines show modified Welch's method for spectral density calculations, with ICEBEAR data in black and RGB data in red. Two broad peaks are identified in all four spectra, with the periods indicated in blue.

irregularity field are reverberating together in a *polyrythm*, with contrasting beats. This phenomenon, which is present in several other PA events that will be analyzed in the future, is not readily explained, though we will attempt to shed some rudimentary light on the issue.

Hosokawa, Motoba, et al. (2010) likewise analyzed coherent scatter (from the Iceland SuperDARN radar) in conjunction with optical observations of pulsating aurora. The authors of that study found that coherent scatter power increased in the dark areas *between* PA patches, and explained this in terms of conductivity enhancements inside the patches, wherein an electric field reduction suppresses irregularity production (Maynard et al., 1973). We can offer some insights into the above, and whether the description is valid also in the present case, using data where the ICEBEAR echo distribution appears with a distinct spatial extent. Figure 5 shows the detailed spatial relationship between a group of ICEBEAR 3D echoes (red) and the transient forms of nearby pulsating patches (green colormap and black contour line). The three top panels show three 3-s intervals, while the three bottom panels show the distribution in auroral intensity (green, left axes) and echo count (red, right axes). The spatial extent of the data in Figure 5 cover roughly 370 km along the y-axis and 280 km along the x-axis. The spatial extent of the echo distribution skirts the regions of relative brightness, corresponding to pulsating patches, confirming inferences in Hosokawa, Motoba, et al. (2010). Since patches are drifting into and out of the area monitored by our instruments, we would expect that the spatial anti-correlation in Figure 5 to be the cause of the temporal anti-correlation we observe in Figure 4. If, for example, the patches drift eastward with a velocity of 500 m/s during an 18-min period, they will have traveled a distance of around 12° in longitude, in line with ICEBEAR's effective field-of-view. Relevant to our claim, this mechanism was likewise evoked by Haldoupis et al. (2003) to explain observed periodicities in mid-latitude E-region radar scatter.
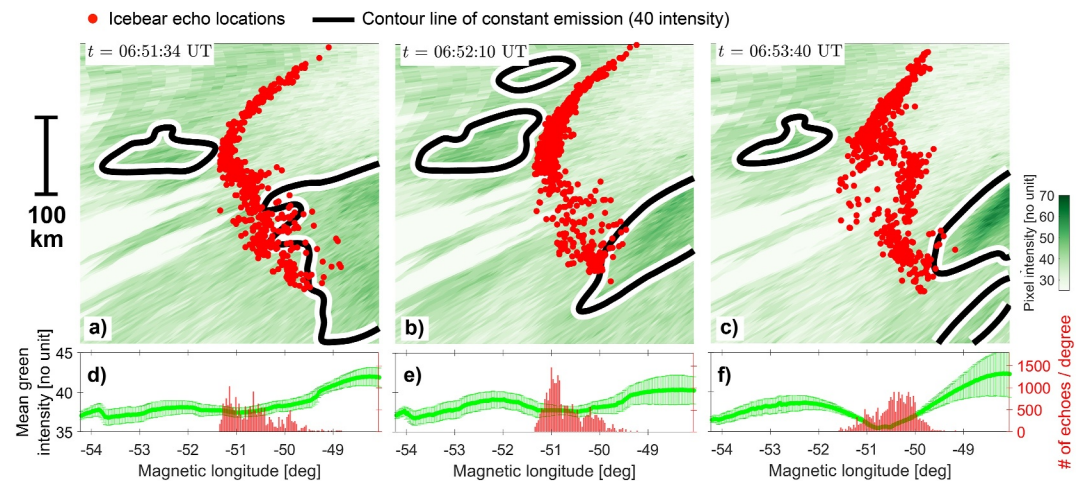
Figure 5. The spatial relationship between auroral emissions and ICEBEAR 3D echoes, in a limited part of the field-of-view. Echoes (red) are superposed on a color-coded map of the auroral emissions (a–c). Panels d–f show the mean green intensity inside the window (green) along with ICEBEAR echo counts (red) per degree longitude. The RGB images are here utilized near the horizon, and the white southwestern protrusions are trees at the Rabbit Lake site.

3.2. Spatial Fluctuations

We will now discuss the co-observed spatial fluctuations, as represented in Figure 6, for each of the three satellites and compare them to the E-region clustering spectra. The first three rows of Figure 6 show *in-situ* observations (along with E-region clustering data from ICEBEAR). The two leftmost columns show detailed timeseries measured by the three Swarm satellites (A, B, and C) during the three conjunctions between perpendicular field fluctuations, electron temperature, and plasma density.

In each of the six PSD panels (two rightmost columns of Figure 6), a solid black line plots the E-region clustering spectrum, along with a log-log linear fit (dashed lines), with the slope (α) indicated. The two spectral density functions are brought to parity by normalizing the area under each graph, which simply entails multiplication by a number. How many turbulence echoes are used in calculating each mean E-region clustering spectrum is indicated with capital N. There are two timebins associated with each conjunction. That is because each conjunction is 105 s long, and we calculate one ICEBEAR 3D spectrum for each clock minute.

The electron temperature measurements by Swarm (panels b, f, and j of Figure 6) reveal elevated temperatures (routinely exceeding 3000 K). The spiky nature of the measured electron temperature is consistent with strong electric field and FAC enhancements and on the edges of pulsating auroral patches (Gillies et al., 2015). These enhancements decrease chemical recombination rates, which ultimately serves to amplify the original electric field enhancements through conductivity modulations (Noël et al., 2005). Note that while we expect the observed temperature spikes to occur on the edges of the auroral structures, we are not able to confirm this by close inspection of the RGB images. The event under consideration is plagued by a light cloud-cover, and it, for the most part, takes place near the south-western horizon of the optical instrument (see Figure 2. Space-ground conjunctions occurring nearer to the instruments' magnetic zenith are more appropriate for this purpose.

3.3. Spatio-Temporal Evolution

A fuller picture of the E-region irregularity landscape is within reach. During the ~25 min period, ICEBEAR observed a total of 44 clustering spectra spread out over 18 one-minute bins (calculated individually from spatially distinct echo populations). In Figure 7 we show 18 mean spectra based on all 44 E-region clustering spectra, with the Swarm-data inserted where appropriate due to a conjunction, using data from Swarm B and C (since observations from satellites A and C are broadly similar). Here, we see how the duration of the conjunctions (105 s) fits neatly into the bigger picture. The one-minute segments near the Swarm-data show a conspicuous tendency to match. The bump, or energy injection point, on display in the Swarm B-conjunctions (Figures 7c and 7d) exhibits profuse evolution throughout the 25 min interval. The bump reaches peak prominence at around
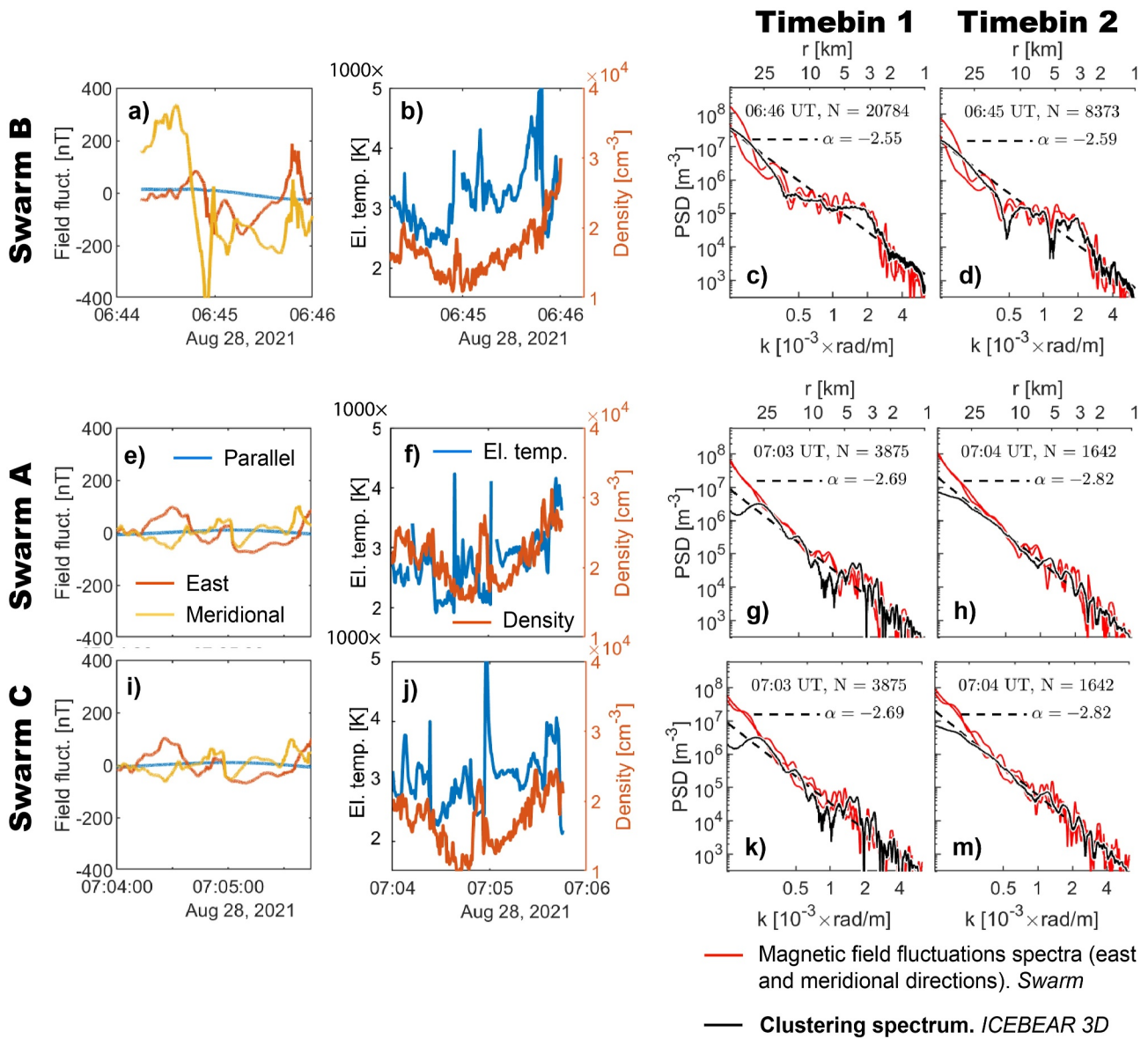
Figure 6. Complete overview of the Swarm timeseries and all spectra calculated during the three conjunctions. The first row shows Swarm B, the second Swarm A, while the third and fourth row show data from Swarm C. Panels (a, e and i) display field-perpendicular magnetic field fluctuations in the mean field-aligned coordinate system. Panels (b, f, and j) display electron temperature (blue, left axis) and electron density (orange, right axis). Panels (c, d, g, h, k, and m) show the Swarm FAC structuring spectrum in red and the ICEBEAR 3D-based E-region echo clustering spectrum in black. Note that the Swarm B conjunction was first studied in (Ivarsen, Lozinsky, et al., 2023).

06:50 UT (when there are no Swarm satellites nearby), before decaying markedly toward the Swarm A + C-conjunctions at around 07:03 UT (see Figure A2 in the Appendix for a brief analysis into this decay).

Based on previous conjunctions, we expect in situ FAC structuring spectra to match ICEBEAR clustering spectra (Ivarsen, Lozinsky, et al., 2023). Nevertheless, it is striking how well the red and black spectra match in Figure 7, both in overall shape and slope. This is especially true for the Swarm B-conjunction (d, e), where the two plots agree both in overall shape and in the small-scale features of the graphs. It is quite clear that the two quantities trace a common signal. We interpret the bump and its evolution as evidence of energy injected by the magnetosphere into the ionosphere at scales around 2–5 km, which then slowly dissipates. In the next section, we shall, in detail, discuss how this process likely unfolds.
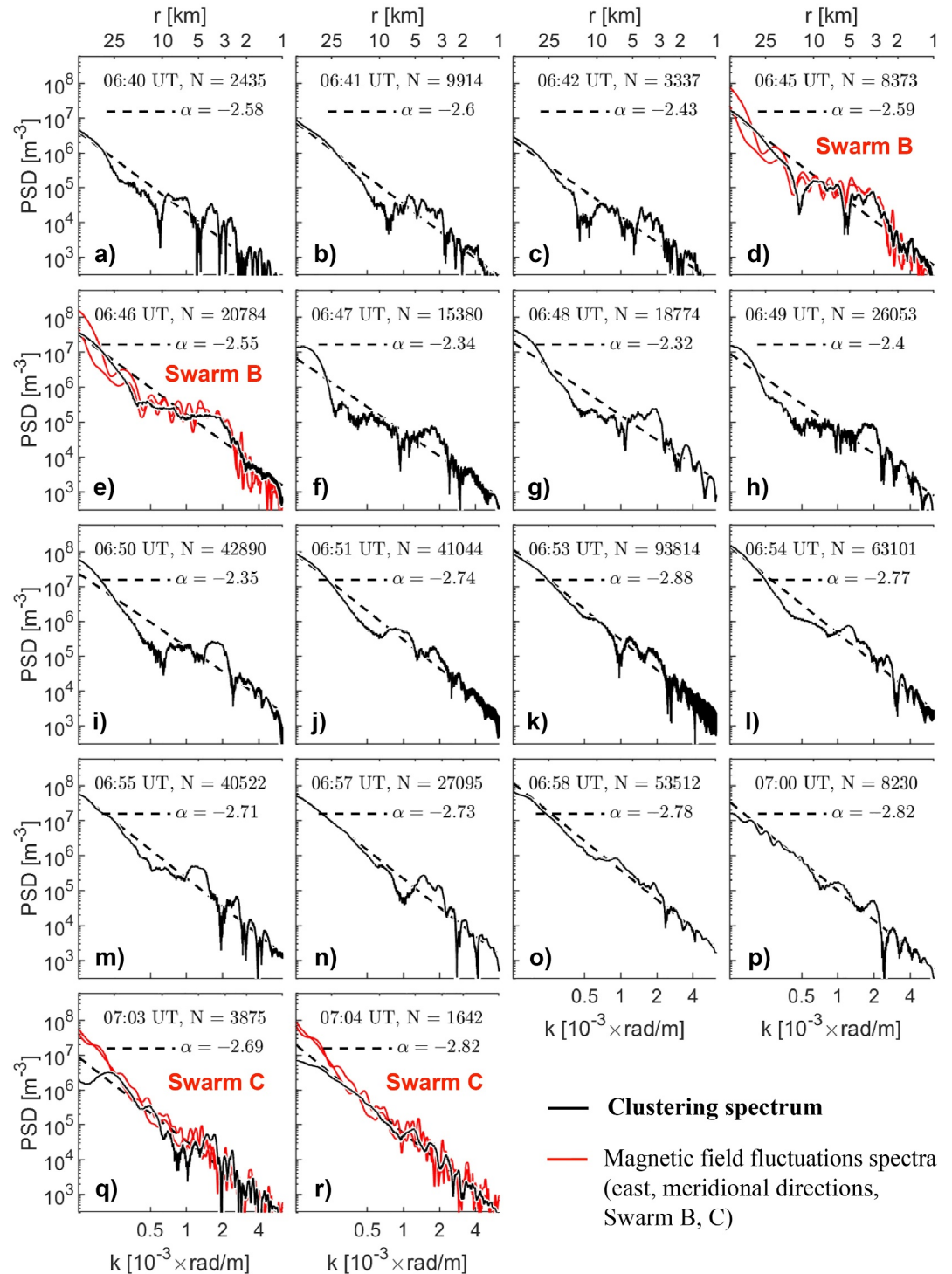
Figure 7. All 18 clustering spectra calculated during the 25 min period considered, presented in sequence, from panel (a) to panel (r). In each panel, a solid black line shows the ICEBEAR 3D clustering spectrum, while a dashed black line shows a log-log linear fit, with the slope value indicated. In panels (d, e, q, and r) two solid red lines show the spectrum of perpendicular magnetic field fluctuations, as measured by Swarm B and C. The two red lines show both the meridional- and east-components of the perpendicular field fluctuations. The top x-axes show spatial scale while the bottom x-axes show corresponding wavenumber. The total number of turbulence echoes correlated to produce each composite spectrum is indicated by N.

4. Discussion and Summary

In this report, we have shown three conjunctions between the Swarm satellites and the ICEBEAR 3D coherent scatter radar. The conjunctions are separated by around 20 min in time, and all occur during the recovery phase of a magnetospheric substorm (Figure 3b). Concurrently, all-sky imager data was recorded by the TREX RGB auroral imager. RGB images confirm the presence of pulsating aurora throughout the area where ICEBEAR 3D echoes occur (Movie S1). An analysis into the temporal fluctuations in both of the ground-based instruments demonstrated that they observe the same signal (Figure 4) for a large share of the measured information.

Figure 6 revealed that the FAC fluctuations, or filamentations, as gleaned in situ by Swarm, exhibit essentially matching turbulent decay of energy per wavevector, as that of the spatial distribution of Farley-Buneman turbulence echoes from the E-region. Figure 5 shows that this turbulence preferentially occurs in the space *between* pulsating patches, in line with expectations from the literature (compare Figures 1 and 5). In a Companion Paper we further explore the topic of spatial anti-correlations in auroral emissions and plasma turbulence (Ivarsen et al., 2024).

A key finding as presented in Figure 7, comes from the ICEBEAR 3D-based E-region clustering spectrum. The two-point correlation analysis of ICEBEAR 3D echo locations gave a spectrum of density irregularity "clustering," a large-scale irregularity spectrum, covering scales between 1 and 25 km. We find a characteristic length scale in the clustering spectra, an injection of energy in terms of power spectral density. Given the preceding temporal analysis, we associate the injection scale directly with electric fields in the pulsating aurora (in the Appendix, we present preliminary statistics for such injection points occurring in ICEBEAR clustering spectra, see Figure A1).

Fundamentally, the clustering spectra observed by ICEBEAR imply that Farley-Buneman waves in the E-region appeared to cluster in space in a similar fashion to that of the spatial structuring, or filamentation, of the field-aligned currents that were concurrently measured. To realize that this constitutes evidence for magnetospheric waves as injectors of 2–5 km wave-energy in the ionosphere's E-region, consider two circumstantial facts. First, the observed FACs here are carried by high-energy precipitating electrons in the PA (Gillies et al., 2015; Nishimura et al., 2020). Second, the PA is driven by chorus wave-particle interactions in the magnetosphere (Kasahara et al., 2018).

To see how chorus wave-electron interactions that occur at great a distance away from the ionosphere's bottomside (and which propagate to the opposite hemisphere after scattering events) can produce a characteristic 2–5 km energy injection into the E-region, consider the mechanism with which Alfvén waves may structure the unstable layer. Impinging Pc-5 pulsations in Earth's magnetic field lines stir up waves that propagate in the *field-perpendicular direction* in the ionospheric electric field. Interference between various wavepackets may then produce fundamental waves that are observable in rocket (Rinnert, 1992) and radar (Foster & Tetenbaum, 1992) experiments, and which carry the characteristics of the waves that produced them (Krane et al., 2000; Rinnert, 1992).

The next step involves the pulsating aurora. Chorus waves cannot penetrate to E-region altitudes, and we require an intermediary. It has been established that the various pulsations in the PA are a result of intermittency in the action of magnetospheric chorus waves (Kasahara et al., 2018). Precipitating electrons (which carry the pulsating aurora) must create a local electric field by charge deposition. The composite variations in this electric field is, together with the pulsating patches themselves, subject to the $E \times B$-drift (Humberset et al., 2018; Yang et al., 2017). Either, the pattern of electron precipitation that is superposed on the ionosphere contains waves of wavelength 2–5 km directly, or it interfers with ambient field structures to form fundamental waveforms in the plasma (Rinnert, 1992). The fast (10–100 Hz) *sub-pulsations* present in the PA likely play an outsize role in producing these kilometer-scale disturbances.

In the large-scale picture, then, the intermittency present in chorus wave interactions are setting up a highly variable (and structured) electric field, which in turn drives a large Poynting flux into the ionosphere (Keiling et al., 2019), which in turn explains the clear bump present in ICEBEAR's clustering spectra (Figure 7): a great amount of energy must dissipate in the diffuse pulsating aurora, the overall most energetic form of aurora, both in terms of particle energy and in the total precipitating energy budget (Newell et al., 2010).

A related possibility involves Alfvén waves pulsations in or around pulsating patches, that modulate the E-region electric field directly, thereby embedding the observed structure (Foster & Tetenbaum, 1992; Rinnert, 1992).

Alfvénic turbulence in the fields that are passed down may account for the 2–5 km injection scale. Whether wave energy or energy carried by precipitating particles dominate the total downward Poynting flux then becomes a central question, and there are clear indications of the outsize role played by the PA in the precipitating energy budget (Newell et al., 2009; Nishimura et al., 2020).

At any rate, the increase in ionization and conductivity associated with the PA serves ultimately to dissipate energy contained in the structured fields that originate in the magnetosphere. For a related point made in relation to the solar wind, we point to Borovsky (2012). The author of that study found no evidence of *mixing*, that is, the dissipation and smoothing out of structured plasma, in the solar wind. In this telling, the dense E-region is where turbulence *goes to die*. Mediated by pressure gradients, the embedded structure is subject to collisional processes in the plasma, and so it will dissipate in the E-region due to ambipolar diffusion and even anomalous diffusion (Braginskii, 1965). In the Appendix, we quantify the decay time associated with the observed E-region turbulence (see Figure A2).

An alternative interpretation to the one presented here involves processes local to the E-region as a cause of FAC structuring. Collisional processes in the ionosphere produce a great deal of secondary low-energy electrons that get trapped below the electron acceleration region in the magnetosphere (Khazanov et al., 2021). Filaments in these thermal electron currents might in turn become observable in the FACs. There could be gradients of ionization brought about by the diffuse precipitating particles, which become gradient-drift unstable, producing kilometer-scale structure *locally* (Cerisier et al., 1985; Greenwald, 1974). The collisional processes that cause secondary electron populations might conceivably be affected by the turbulent cascade, and so the locally grown instabilities might structure the return currents. In other words, the black and red spectra in Figure 7 could conceivably all be driven by processes local to the E-region. That the injection scale we observe (2–5 km) is favored for the gradient drift instability (Tsunoda, 1988) speaks for this interpretation. As a counterpoint, E-region conductivities will be highly elevated due to the intense high-energy electron precipitation associated with the pulsating aurora (Hosokawa, Tsugawa, et al., 2010), potentially shorting out kilometer scale irregularities (Vickrey & Kelley, 1982). Nevertheless, further efforts are needed to assess the degree to which small-scale turbulence in the E-region is exerting a significant feedback on the ionosphere-magnetosphere system (e.g., Wiltberger et al., 2017).

Lastly, we must address an altogether surprising find in the present study. We saw here a possibly characteristic behavior of local enhancements in the echo detection rate lagging local intensifications in auroral emissions by several minutes, in this Case 6 min (Figure 4b). Although we only show one example herein, this behavior is observed in several other cases with different lags, typically on the order of several minutes. The lag-effect is associated with a cyclical temporal anti-correlation between the two quantities. This may be seen in context of the spatial anti-correlation that exists between the two quantities (Figure 5), which may translate into a temporal anti-correlation as the pulsating patches drift into and out of the field-of-view (Haldoupis et al., 2003). Anti-correlation in intensity (amplitude) notwithstanding, Figure 4c demonstrates that the observed pulsations (frequency) are highly correlated between the data sets.

The present study demonstrates the capabilities of the new ICEBEAR 3D data set in uncovering fundamental truths about electrojet turbulence and about the ionosphere-magnetosphere interaction in general. That electric fields set up in the magnetosphere can structure the ionosphere directly has been suggested before by (Keiling et al., 2019; Taguchi et al., 1995). However, seldom has this been shown so clearly and succinctly.

We expect that future studies using ICEBEAR 3D observations, in conjunction with the RGB TREX imager, will contribute toward a comprehensive understanding of magnetosphere-ionosphere interactions. Such efforts must also including modeling (Sarris, 2019). The continuous monitoring of geospace above Rabbit Lake by ICEBEAR 3D and the RGB TREX all-sky imager present an excellent opportunity for enhanced magnetosphere-ionosphere understanding in the future.

Appendix A: Spectral Injection Points

The spectral injection, or bump, on display in Figures 6 and 7 can be characterized by their contrasts, or amplitudes, relative to a linear (in log-log representation) curve fit. As working definition, we identify such injection points if their peak value exceeds 150% of the linear fit value.
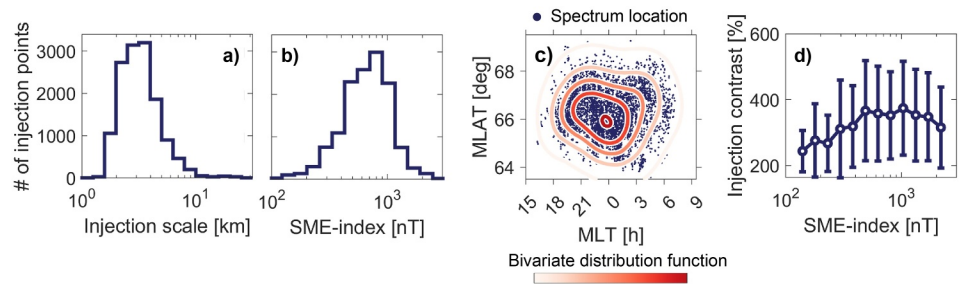
Figure A1. 13,700 injection points, identified in 4700 E-region clustering spectra. Each injection point is identified as a peak in spectral power that extends at least 150% above a log-log linear fit of the spectrum in question. The first two panels show the injection points binned by injection scale size (a) and SME-index value at time of observation (b). Panel (c) plots the geospatial locations of each spectra in dark blue dots, along with bivariate distribution function in a red colorscale. Panel(d) shows the mean injection contrast in % of the log-log linear fit value.

In Figure A1 we show preliminary statistics of all spectral injection points found in ICEBEAR 3D spectra calculated during 2020 and 2021. The figure shows 13,700 injection points, ordered by injection scale size (panel a), SME-index at the time of observation (panel b), the location in geospace of the observation (panel c), and the injection contrast or amplitude (panel d). The injection scale sizes are typically found at 2–5 km, in accordance with the results we report here. The magnetic local time distribution (Figure A1c) is likely to be influenced by the radar field-of-view: ICEBEAR's beam configuration means it detects echoes primarily at magnetic latitudes between 64° and 68°, favoring midnight with an expanded auroral oval (Ivarsen, St-Maurice, Hussey, Galeschuk, et al., 2023). However, the peak of the distribution in Figure A1c is highly reminiscent of substorm onset distributions (Figure 1 in Milan et al., 2010, e.g.). Seen in context with Figure 3, we surmise that the 2–5 km injection points frequently observed by ICEBEAR 3D are associated, at least observationally, with the substorm cycle.

A1. Decay Times

Recently, Troyer et al. (2024) quantified the decay time in chorus wave activity following magnetospheric substorms, with one aim being that of strengthening the causal association between chorus waves and the energetic particle precipitation present in the pulsating aurora. The authors found that, in the midnight sector, the resonant wave power in measured chorus wave interactions decay on average with a *e*-folding time of around 25 min (see Figure 2 in Troyer et al., 2024). In the present paper, we argue that the spectral injection on display in Figure 7 is driven by the pulsating aurora, and so we expect the relaxation time associated with this energy injection to match that of the underlying cause mechanism: chorus wave activity.

In the 18 spectra from Figure 7, we identify 48 injection points. Figure A2a shows their average contrast, or amplitude, for each clock minute with ICEBEAR 3D data during the event studied, with errorbars denoting standard deviations. A solid black line plots an exponential fit, $\eta = a_0 \times e^{-t/\tau}$, where η represents injection contrast, a_0 is a scaling parameter, and $\tau = 22$ min Figure A2b plots the log-log linear slope (spectral index) for each of the 18 spectra from Figure 7, demonstrating how spectra tended to *steepen* as the 2–5 km injection power faded away. We thus find that the 2–5 km injection point on display in Figure 7 fades away with an *e*-folding that matches the rate at which the resonant chorus wave power decays (Troyer et al., 2024), providing circumstantial evidence for our main conclusions.
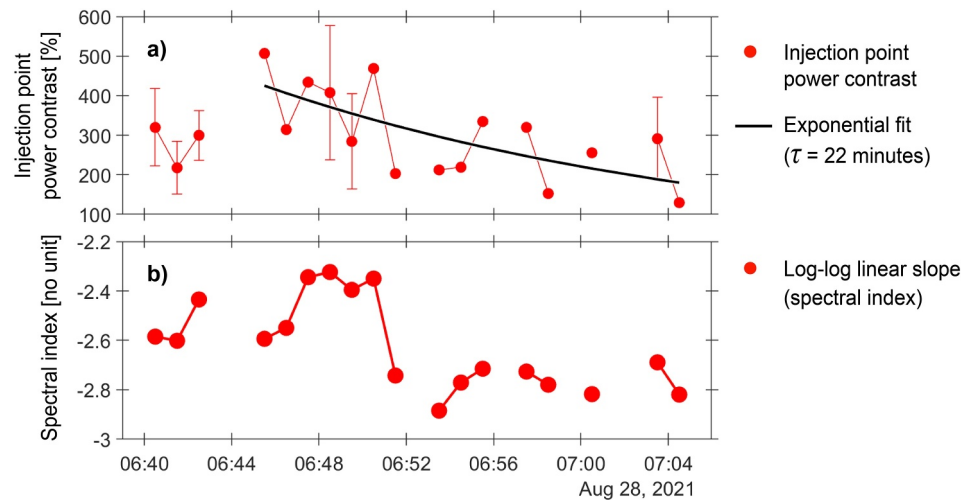
Figure A2. Injection point power contrast (a) and log-log linear slope (b) for all 18 clustering spectra shown in Figure 4 in the main paper.

Data Availability Statement

ICEBEAR 3D echo data for 2020, 2021 is published with https://doi.org/10.5281/zenodo.7509022 (Hussey & Ivarsen, 2023). Data from the European Space Agency's Swarm mission can accessed at https://swarm-diss.eo.esa.int/ (Swarm, 2023). SuperMAG data can be accessed at https://supermag.jhuapl.edu/mag/. TREX RGB imager data can be accessed at http://data.phys.ucalgary.ca (RGB, 2023).

References

Baker, K. B., & Wing, S. (1989). A new magnetic coordinate system for conjugate studies at high latitudes. *Journal of Geophysical Research*, *94*(A7), 9139–9143. https://doi.org/10.1029/JA094iA07p09139

Basu, S., Basu, S., MacKenzie, E., Coley, W. R., Hanson, W. B., & Lin, C. S. (1984). F region electron density irregularity spectra near auroral acceleration and shear regions. *Journal of Geophysical Research*, *89*(A7), 5554–5564. https://doi.org/10.1029/JA089iA07p05554

Billett, D. D., Perry, G. W., Clausen, L. B. N., Archer, W. E., McWilliams, K. A., Haaland, S., et al. (2021). The relationship between large scale thermospheric density enhancements and the spatial distribution of poynting flux. *Journal of Geophysical Research: Space Physics, n/a*, *126*(n/a), e2021JA029205. https://doi.org/10.1029/2021JA029205

Bland, E., Tesema, F., & Partamies, N. (2021). D-region impact area of energetic electron precipitation during pulsating aurora. *Annales Geophysicae*, *39*(1), 135–149. https://doi.org/10.5194/angeo-39-135-2021

Borovsky, J. E. (2012). Looking for evidence of mixing in the solar wind from 0.31 to 0.98 AU. *Journal of Geophysical Research*, *117*(A6). https://doi.org/10.1029/2012JA017525

Braginskii, S. I. (1965). Transport processes in a plasma. *Reviews of plasma physics*, *1*, 205. Retrieved from http://adsabs.harvard.edu/abs/1965RvPP...1..205B

Buneman, O. (1963). Excitation of field aligned sound waves by electron streams. *Physical Review Letters*, *10*(7), 285–287. https://doi.org/10.1103/PhysRevLett.10.285

Cerisier, J. C., Berthelier, J. J., & Beghin, C. (1985). Unstable density gradients in the high-latitude ionosphere. *Radio Science*, *20*(4), 755–761. https://doi.org/10.1029/RS020i004p00755

Farley, D. T. (1969). Incoherent scatter correlation function measurements. *Radio Science*, *4*(10), 935–953. https://doi.org/10.1029/RS004i010p00935

Feynman, R. P., & Sands, M. L. (1963). *The Feynman lectures on physics*. Addison-Wesley Pub. Co.

Forsyth, C., Rae, I. J., Coxon, J. C., Freeman, M. P., Jackman, C. M., Gjerloev, J., & Fazakerley, A. N. (2015). A new technique for determining substorm onsets and phases from indices of the electrojet (SOPHIE). *Journal of Geophysical Research: Space Physics*, *120*(12), 10592–10606. https://doi.org/10.1002/2015JA021343

Foster, J. C., & Tetenbaum, D. (1992). Phase velocity studies of 34-cm E-region irregularities observed at Millstone Hill. *Journal of Atmospheric and Terrestrial Physics*, *54*(6), 759–768. https://doi.org/10.1016/0021-9169(92)90114-Z

Friis-Christensen, E., Lühr, H., & Hulot, G. (2006). Swarm: A constellation to study the Earth's magnetic field. *Earth Planets and Space*, *58*(4), BF03351933. https://doi.org/10.1186/BF03351933

Gillies, D. M., Knudsen, D., Spanswick, E., Donovan, E., Burchill, J., & Patrick, M. (2015). Swarm observations of field-aligned currents associated with pulsating auroral patches. *Journal of Geophysical Research: Space Physics*, *120*(11), 9484–9499. https://doi.org/10.1002/2015JA021416

Gillies, D. M., Liang, J., Donovan, E., & Spanswick, E. (2020). The apparent motion of STEVE and the picket fence phenomena. *Geophysical Research Letters*, *47*(20), e2020GL088980. https://doi.org/10.1029/2020GL088980

Greenwald, R. A. (1974). Diffuse radar aurora and the gradient drift instability. *Journal of Geophysical Research (1896-1977)*, *79*(31), 4807–4810. https://doi.org/10.1029/JA079i031p04807

Grono, E., & Donovan, E. (2018). Differentiating diffuse auroras based on phenomenology. *Annales Geophysicae*, *36*(3), 891–898. https://doi.org/10.5194/angeo-36-891-2018

Grono, E., & Donovan, E. (2020). Surveying pulsating auroras. *Annales Geophysicae*, *38*(1), 1–8. https://doi.org/10.5194/angeo-38-1-2020

Guizar-Sicairos, M., & Gutiérrez-Vega, J. C. (2004). Computation of quasi-discrete Hankel transforms of integer order for propagating optical wave fields. *JOSA A*, *21*(1), 53–58. https://doi.org/10.1364/JOSAA.21.000053

Haldoupis, C., Bourdillon, A., Kamburelis, A., Hussey, G. C., & Koehler, J. A. (2003). 50 MHz continuous wave interferometer observations of the unstable mid-latitude E-region ionosphere. *Annales Geophysicae*, *21*(7), 1589–1600. https://doi.org/10.5194/angeo-21-1589-2003

Hosokawa, K., Miyoshi, Y., Ozaki, M., Oyama, S.-I., Ogawa, Y., Kurita, S., et al. (2020). Multiple time-scale beats in aurora: Precise orchestration via magnetospheric chorus waves. *Scientific Reports*, *10*(1), 3380. https://doi.org/10.1038/s41598-020-59642-8

Hosokawa, K., Motoba, T., Yukimatu, A. S., Milan, S. E., Lester, M., Kadokura, A., et al. (2010). Plasma irregularities adjacent to auroral patches in the postmidnight sector. *Journal of Geophysical Research*, *115*(A9). https://doi.org/10.1029/2010JA015319

Hosokawa, K., & Ogawa, Y. (2010). Pedersen current carried by electrons in auroral D-region. *Geophysical Research Letters*, *37*(18). https://doi.org/10.1029/2010GL044746

Hosokawa, K., & Ogawa, Y. (2015). Ionospheric variation during pulsating aurora. *Journal of Geophysical Research: Space Physics*, *120*(7), 5943–5957. https://doi.org/10.1002/2015JA021401

Hosokawa, K., Tsugawa, T., Shiokawa, K., Otsuka, Y., Nishitani, N., Ogawa, T., & Hairston, M. R. (2010). Dynamic temporal evolution of polar cap tongue of ionization during magnetic storm. *Journal of Geophysical Research*, *115*(A12). https://doi.org/10.1029/2010JA015848

Huba, J. D., Hassam, A. B., Schwartz, I. B., & Keskinen, M. J. (1985). Ionospheric turbulence: Interchange instabilities and chaotic fluid behavior. *Geophysical Research Letters*, *12*(1), 65–68. https://doi.org/10.1029/GL012i001p00065

Humberset, B. K., Gjerloev, J. W., Mann, I. R., Michell, R. G., & Samara, M. (2018). On the persistent shape and coherence of pulsating auroral patches. *Journal of Geophysical Research: Space Physics*, *123*(5), 4272–4289. https://doi.org/10.1029/2017JA024405

Hussey, G., & Ivarsen, M. (2023). ICEBEAR 3D coherent scatter radar data for 2020, 2021 [DATA]. *Zenodo*. https://doi.org/10.5281/zenodo.7509022

Huyghebaert, D., Hussey, G., Vierinen, J., McWilliams, K., & St-Maurice, J.-P. (2019). Icebear: An all-digital bistatic coded continuous-wave radar for studies of the E region of the ionosphere. *Radio Science*, *54*(4), 349–364. https://doi.org/10.1029/2018RS006747

Huyghebaert, D., St.-Maurice, J.-P., McWilliams, K., Hussey, G., Howarth, A. D., Rutledge, P., & Erion, S. (2021). The properties of ICEBEAR E-region coherent radar echoes in the presence of near infrared auroral emissions, as measured by the Swarm-E fast auroral imager. *Journal of Geophysical Research: Space Physics*, *126*(12), e2021JA029857. https://doi.org/10.1029/2021JA029857

Ivarsen, M. F., Bull, P., Llinares, C., & Mota, D. F. (2016). Distinguishing screening mechanisms with environment-dependent velocity statistics. *Astronomy and Astrophysics*, *595*, A40. https://doi.org/10.1051/0004-6361/201628604

Ivarsen, M. F., Gilles, D. M., Huyghebaert, D. R., St-Maurice, J. P., Lozinsky, A., Galeschuk, D., & Hussey, G. (2024). Turbulence embedded into the ionosphere by electromagnetic waves. *Submitted to JGR: Space Physics*.

Ivarsen, M. F., Jin, Y., Spicher, A., St-Maurice, J.-P., Park, J., & Billett, D. (2023). GNSS scintillations in the Cusp, and the role of precipitating particle energy fluxes. *Journal of Geophysical Research: Space Physics*, *128*(10), e2023JA031849. https://doi.org/10.1029/2023JA031849

Ivarsen, M. F., Lozinsky, A., St-Maurice, J.-P., Spicher, A., Huyghebaert, D., Hussey, G. C., et al. (2023). The distribution of small-scale irregularities in the E-region, and its tendency to match the spectrum of field-aligned current structures in the F-region. *Journal of Geophysical Research: Space Physics*, *128*(5), e2022JA031233. https://doi.org/10.1029/2022JA031233

Ivarsen, M. F., Park, J., Kwak, Y.-S., Jin, Y., Knudsen, D. J., & Clausen, L. B. N. (2020). Observational evidence for the role of hall conductance in Alfvén wave reflection. *Journal of Geophysical Research: Space Physics*, *125*(12), e2020JA028119. https://doi.org/10.1029/2020JA028119

Ivarsen, M. F., St-Maurice, J.-P., Hussey, G., Spicher, A., Jin, Y., Lozinsky, A., et al. (2023). Measuring small-scale plasma irregularities in the high-latitude E- and F-regions simultaneously. *Scientific Reports*, *13*(1), 11579. https://doi.org/10.1038/s41598-023-38777-4

Ivarsen, M. F., St-Maurice, J.-P., Hussey, G. C., Galeschuk, D., Lozinsky, A., Pitzel, B., & McWilliams, K. A. (2023). An algorithm to separate ionospheric turbulence radar echoes from those of meteor trails in large data sets. *Journal of Geophysical Research: Space Physics*, *128*(1), e2022JA031050. https://doi.org/10.1029/2022JA031050

Jin, Y., Clausen, L. B. N., Spicher, A., Ivarsen, M. F., Zhang, Y., Miloch, W. J., & Moen, J. I. (2021). Statistical distribution of decameter scale (50 m) ionospheric irregularities at high latitudes. *Geophysical Research Letters*, *48*(19), e2021GL094794. https://doi.org/10.1029/2021GL094794

Jones, S. L., Lessard, M. R., Rychert, K., Spanswick, E., & Donovan, E. (2011). Large-scale aspects and temporal evolution of pulsating aurora. *Journal of Geophysical Research*, *116*(A3). https://doi.org/10.1029/2010JA015840

Kasahara, S., Miyoshi, Y., Yokota, S., Mitani, T., Kasahara, Y., Matsuda, S., et al. (2018). Pulsating aurora from electron scattering by chorus waves. *Nature*, *554*(7692), 337–340. https://doi.org/10.1038/nature25505

Kawamura, Y., Hosokawa, K., Nozawa, S., Ogawa, Y., Kawabata, T., Oyama, S.-I., et al. (2020). Estimation of the emission altitude of pulsating aurora using the five-wavelength photometer. *Earth Planets and Space*, *72*(1), 96. https://doi.org/10.1186/s40623-020-01229-8

Keiling, A., Thaller, S., Wygant, J., & Dombeck, J. (2019). Assessing the global Alfvén wave power flow into and out of the auroral acceleration region during geomagnetic storms. *Science Advances*, *5*(6), eaav8411. https://doi.org/10.1126/sciadv.aav8411

Khazanov, G. V., Glocer, A., & Chu, M. (2021). Electron energy interplay in the geomagnetic trap below the auroral acceleration region. *Journal of Geophysical Research: Space Physics*, *126*(5), e2020JA028811. https://doi.org/10.1029/2020JA028811

Kintner, P. M., & Seyler, C. E. (1985). The status of observations and theory of high latitude ionospheric and magnetospheric plasma turbulence. *Space Science Reviews*, *41*(1–2), 91–129. https://doi.org/10.1007/BF00241347

Krane, B., Pécseli, H. L., Trulsen, J., & Primdahl, F. (2000). Spectral properties of low-frequency electrostatic waves in the ionospheric E region. *Journal of Geophysical Research*, *105*(A5), 10585–10601. https://doi.org/10.1029/1999JA900503

Laundal, K. M., Hatch, S. M., & Moretto, T. (2019). Magnetic effects of plasma pressure gradients in the upper F region. *Geophysical Research Letters*. https://doi.org/10.1029/2019GL081980

Lessard, M. R. (2012). A review of pulsating aurora. In *Auroral phenomenology and magnetospheric processes: Earth and other planets* (pp. 55–68). American Geophysical Union (AGU). https://doi.org/10.1029/2011GM001187

Lorentzen, D. A., Moen, J., Oksavik, K., Sigernes, F., Saito, Y., & Johnsen, M. G. (2010). In situ measurement of a newly created polar cap patch. *Journal of Geophysical Research*, *115*(A12). https://doi.org/10.1029/2010JA015710

Lozinsky, A., Hussey, G., McWilliams, K., Huyghebaert, D., & Galeschuk, D. (2022). ICEBEAR-3D: A low elevation imaging radar using a non-uniform coplanar receiver array for E region observations. *Radio Science*, *57*(3), e2021RS007358. https://doi.org/10.1029/2021RS007358

Maynard, N. C., Bahnsen, A., Christophersen, P., Egeland, A., & Lundin, R. (1973). An example of anticorrelation of auroral particles and electric fields. *Journal of Geophysical Research*, *78*(19), 3976–3980. https://doi.org/10.1029/JA078i019p03976

Milan, S. E., Grocott, A., & Hubert, B. (2010). A superposed epoch analysis of auroral evolution during substorms: Local time of onset region. *Journal of Geophysical Research*, *115*(A5). https://doi.org/10.1029/2010JA015663

Milan, S. E., Hosokawa, K., Lester, M., Sato, N., Yamagishi, H., & Honary, F. (2008). D region HF radar echoes associated with energetic particle precipitation and pulsating aurora. *Annales Geophysicae*, *26*(7), 1897–1904. https://doi.org/10.5194/angeo-26-1897-2008

Mounir, H., Berthelier, A., Cerisier, J. C., Lagoutte, D., & Beghin, C. (1991). The small-scale turbulent structure of the high latitude ionosphere - Arcad-Aureol-3 observations. *Annales Geophysicae*, *9*, 725–737. Retrieved from http://adsabs.harvard.edu/abs/1991AnGeo...9..725M

Newell, P. T., & Gjerloev, J. W. (2011a). Evaluation of SuperMAG auroral electrojet indices as indicators of substorms and auroral power. *Journal of Geophysical Research*, *116*(A12). https://doi.org/10.1029/2011JA016779

Newell, P. T., & Gjerloev, J. W. (2011b). Substorm and magnetosphere characteristic scales inferred from the SuperMAG auroral electrojet indices. *Journal of Geophysical Research*, *116*(A12). https://doi.org/10.1029/2011JA016936

Newell, P. T., Sotirelis, T., & Wing, S. (2009). Diffuse, monoenergetic, and broadband aurora: The global precipitation budget. *Journal of Geophysical Research*, *114*(A9). https://doi.org/10.1029/2009JA014326

Newell, P. T., Sotirelis, T., & Wing, S. (2010). Seasonal variations in diffuse, monoenergetic, and broadband aurora. *Journal of Geophysical Research*, *115*(A3). https://doi.org/10.1029/2009JA014805

Nishimura, Y., Lessard, M. R., Katoh, Y., Miyoshi, Y., Grono, E., Partamies, N., et al. (2020). Diffuse and pulsating aurora. *Space Science Reviews*, *216*(1), 4. https://doi.org/10.1007/s11214-019-0629-3

Noël, J.-M. A., St. Maurice, J.-P., & Blelly, P.-L. (2005). The effect of *E*-region wave heating on electrodynamical structures. *Annales Geophysicae*, *23*(6), 2081–2094. https://doi.org/10.5194/angeo-23-2081-2005

Park, J., Lühr, H., Knudsen, D. J., Burchill, J. K., & Kwak, Y.-S. (2017). Alfvén waves in the auroral region, their Poynting flux, and reflection coefficient as estimated from Swarm observations. *Journal of Geophysical Research: Space Physics*, *122*(2), 2345–2360. https://doi.org/10.1002/2016JA023527

RGB, T. (2023). UCalgary space remote sensing group data landing page — UCalgary SRS data documentation [DATA]. *RGB*. https://doi.org/10.11575/4P8E-1K65

Rinnert, K. (1992). Plasma waves observed in the auroral E-region - ROSE campaign. *Journal of Atmospheric and Terrestrial Physics*, *54*(6), 683–692. https://doi.org/10.1016/0021-9169(92)90106-U

Ritter, P., Lühr, H., & Rauberg, J. (2013). Determining field-aligned currents with the Swarm constellation mission. *Earth Planets and Space*, *65*(11), 9–1294. https://doi.org/10.5047/eps.2013.09.006

Sarris, T. E. (2019). Understanding the ionosphere thermosphere response to solar and magnetospheric drivers: Status, challenges and open issues. *Philosophical Transactions of the Royal Society A: Mathematical, Physical & Engineering Sciences*, *377*(2148), 20180101. https://doi.org/10.1098/rsta.2018.0101

Spicher, A., LaBelle, J., Bonnell, J. W., Roglans, R., Moser, C., Fuselier, S. A., et al. (2022). Interferometric study of ionospheric plasma irregularities in regions of phase scintillations and HF backscatter. *Geophysical Research Letters*, *49*(12), e2021GL097013. https://doi.org/10.1029/2021GL097013

Swarm. (2023). Swarm data access [DATA]. *Swarm*. Retrieved from https://swarm-diss.eo.esa.int/

Taguchi, S., Sugiura, M., Iyemori, T., Winningham, J. D., & Slavin, J. A. (1995). Highly structured ionospheric convection for northward interplanetary magnetic field: A case study with DE 2 observations. *Journal of Geophysical Research*, *100*(A8), 14743–14753. https://doi.org/10.1029/94JA03373

Tröbs, M., & Heinzel, G. (2006). Improved spectrum estimation from digitized time series on a logarithmic frequency axis. *Measurement*, *39*(2), 120–129. https://doi.org/10.1016/j.measurement.2005.10.010

Troyer, R. N., Jaynes, A. N., Hartley, D. P., Meredith, N. P., Hua, M., & Bortnik, J. (2024). Substorm driven chorus waves: Decay timescales and implications for pulsating aurora. *Journal of Geophysical Research: Space Physics*, *129*(1), e2023JA031883. https://doi.org/10.1029/2023JA031883

Tsunoda, R. T. (1988). High-latitude F region irregularities: A review and synthesis. *Reviews of Geophysics*, *26*(4), 719–760. https://doi.org/10.1029/RG026i004p00719

VanderPlas, J. T. (2018). Understanding the Lomb–Scargle periodogram. *The Astrophysical Journal - Supplement Series*, *236*(1), 16. https://doi.org/10.3847/1538-4365/aab766

Vickrey, J. F., & Kelley, M. C. (1982). The effects of a conducting E layer on classical F region cross-field plasma diffusion. *Journal of Geophysical Research*, *87*(A6), 4461–4468. https://doi.org/10.1029/JA087iA06p04461

Wiltberger, M., Merkin, V., Zhang, B., Toffoletto, F., Oppenheim, M., Wang, W., et al. (2017). Effects of electrojet turbulence on a magnetosphere-ionosphere simulation of a geomagnetic storm. *Journal of Geophysical Research: Space Physics*, *122*(5), 5008–5027. https://doi.org/10.1002/2016JA023700

Yang, B., Donovan, E., Liang, J., & Spanswick, E. (2017). A statistical study of the motion of pulsating aurora patches: Using the THEMIS all-sky imager. *Annales Geophysicae*, *35*(2), 217–225. https://doi.org/10.5194/angeo-35-217-2017